Advanced Materials

ADVANCED MATERIALS
www.advmat.de

RESEARCH ARTICLE

Multifunctional Ferroelectric Bioelectronic Interfaces for Long-Term Biosafe Vagus Nerve Modulation

Xule Zhu[1,2] | Qilong Zhao[1] | Yun Wang[3] | Xuemin Du[1,2]

[1]State Key Laboratory of Biomedical Imaging Science and System, Center For Intelligent Biomedical Materials and Devices (IBMD), Shenzhen Institutes of Advanced Technology (SIAT), Chinese Academy of Sciences (CAS), Shenzhen, China | [2]University of Chinese Academy of Sciences, Beijing, China | [3]Neuroscience Research Institute and Department of Neurobiology, School of Basic Medical Sciences, Key Laboratory for Neuroscience, PKU-IDG/McGovern Institute for Brain Research, Ministry of Education/National Health Commission and State Key Laboratory of Natural and Biomimetic Drugs, Peking University, Beijing, China

Correspondence: Xuemin Du (xm.du@siat.ac.cn)

Received: 23 December 2025 | **Revised:** 12 March 2026 | **Accepted:** 31 March 2026

ABSTRACT

Implantable bioelectronics offer precise control of neural activity and hold great therapeutic potential for neurological diseases and refractory autoimmune disorders. However, conventional implants suffer from non-adaptive nerve interfaces, including geometric mismatch, suture-related trauma, and absence of neuron-like bioelectrical signals, which significantly undermine their long-term biosafety and efficacy. Here we present a multifunctional ferroelectric bioelectronic interface (FBI) that integrates a bilayer natural polymer-based hydrogel, ferroelectric poly(vinylidene fluoride-*co*-trifluoro ethylene) (P(VDF-TrFE)) polymer, and photothermal carbon nanotubes (CNT), imparting unprecedented synergistic functions, including self-rolling geometric matching, strong interfacial adhesion that eliminates the need for suturing, and neuron-mimetic polarization-change-induced bioelectrical signaling. When applied to the vagus nerves, this adaptive FBI enables near-infrared-mediated neuromodulation that effectively reduces pro-inflammatory cytokine levels. Compared with conventional vagus nerve modulators, such innovative FBI avoids nerve compression, minimizes focal inflammation, and maintains persistent neuromodulation efficacy during long-term implantation. By integrating precise geometric adaptability, seamless bioadhesive fixation, bioelectrical biomimicry, and robust biosafety, the FBI platform offers a new paradigm for next-generation implantable bioelectronics for durable nerve modulation and treatment of neurological and autoimmune conditions.

1 | Introduction

Implantable bioelectronics have been widely applied for neuromodulation across the peripheral to central nervous systems, offering remarkable therapeutic opportunities for disorders inadequately addressed by existing clinical approaches [1–4]. Autoimmune disorders such as endotoxemia, sepsis, rheumatoid arthritis, and inflammatory bowel disease affect near 5% of the global population, yet durable suppression of pro-inflammatory cytokines remains challenging due to the limited efficacy of available drugs and interventional options [5]. Vagus nerve-targeted implants can modulate the neuroimmune axis through established peripheral nerve system-immune interactions, thereby attenuating pro-inflammatory cytokine release and offering promising strategies for treating autoimmune diseases [6–8]. However, translational success depends on long-term biosafe and reliable interface requirements that current devices fail to meet due to non-adaptive nerve interfacing [9, 10].

Xule Zhu and Qilong Zhao contributed equally to this work.

Conventional vagus nerve modulators typically use metallic cuff electrodes, which are poorly matched to the delicate and fragile structure of vagus nerve [11–14]. First, standard cuff geometries fail to conform to the diverse vagal fascicular architectures and therefore require mechanical locking to maintain contact; this induces tissue compression and local inflammation [15–17]. Second, device displacement during movement is common and usually countered by surgical suturing, a procedure that is particularly problematic for fine peripheral nerves ($\varphi <$ 0.6 mm), causing unavoidable tissue trauma and potential complications [18]. Third, signal delivery in these devices relies solely on electronic stimulation, which fundamentally differs from the polarization change-induced bioelectrical cues that naturally elicit neuronal responses; this mismatch leads to limited penetration, reduced signal fidelity, and electrochemical cytotoxicity [19, 20]. Recent polymer-based bioelectronics incorporating shape-memory polymers, mechanically compliant hydrogels, and photovoltaic polymers have shown promise in alleviating certain aspects of the nerve-device mismatches [21–36]. Nevertheless, existing interfaces still lack the integrated functionality of active geometric compliance, sutureless implantation, and adaptive neuron-like bioelectrical communication. This absence of functional synergy prevents truly adaptive interfacing with fine vagus nerves and constrains the clinical potential of bioelectronic modulation for autoimmune disease treatment [37, 38].

Here, we report a multifunctional ferroelectric bioelectronic interface (FBI) that integrates self-rolling geometry, robust interfacial adhesion, and neuron-like polarization-induced bioelectrical signal to enable adaptive, long-term, biosafe, and reliable vagus nerve modulation (Figure 1). The FBI comprises two functional material layers: (1) a natural polymer-based hydrogel bilayer (i.e., a bottom chitosan layer and an upper calcium-ion-crosslinked, *N*-hydroxysuccinimide (NHS)-functionalized alginate (Alg-NHS) layer), which imparts self-rolling behavior and strong interfacial adhesion; and (2) a ferroelectric layer of P(VDF-TrFE) polymer stripe arrays with an underside electrosprayed CNT/P(VDF-TrFE) coating that generates bioelectrical signals. Through the synergistic action of these components, the FBI achieves exceptional adaptability at the vagus nerve interface, enabling sutureless implantation with conformal, seamless contact and near-infrared-mediated neuromodulation that effectively suppresses pro-inflammatory cytokines. In freely moving rats, the FBI demonstrates durable biosafety and reliability, with no nerve oppression, negligible local inflammation, and sustained anti-inflammatory efficacy over long-term implantation. By integrating precise geometric adaptability, seamless bioadhesive fixation, bioelectrical biomimicry, and robust biosafety, the FBI platform offers a new paradigm for next-generation implantable bioelectronics for durable nerve modulation and treatment of neurological and autoimmune conditions.

2 | Results

2.1 | Design of FBI

The FBI comprises a bilayer natural hydrogel substrate integrated with ferroelectric bioelectronics through a rationally componential and structural design (Figure 2A). Alg-NHS and chitosan are selected to form the hydrogel bilayer because of their excellent biocompatibility and mechanical compliance with nerve tissues [39]. Biocompatible P(VDF-TrFE) and CNT are designed to form the upper ferroelectric polymer layer due to their intrinsic ferroelectric and photothermal effects [40–42]. To fabricate the FBI, we first prepare a P(VDF-TrFE) film by casting a precursor solution into a prefabricated silicon mold featuring inverse micropyramid arrays, followed by polarization of the film. CNT/P(VDF-TrFE) microparticles are then deposited onto the bottom surface of the film via electrospraying to form an interlayer. The resulting composite film is cut into stripe arrays. Subsequently, Alg-NHS and chitosan hydrogel precursors are sequentially cast onto the CNT/P(VDF-TrFE) interlayer of the composite film, followed by ionic crosslinking and air drying. This process yields the FBI in its initial form of flattened film with a well-defined hierarchical multilayer structure (Figure 2A–C; Figure S1, see details in Experimental Section). The ferroelectric CNT/P(VDF-TrFE) stripes are alternately arranged onto the bilayer hydrogel substrate, enabling contact with target nerve bundles without disturbing morphing freedom (Figure 2A). Cellular-scale micropyramid arrays are designed on the surface of the FBI (Figure S1), which can enhance neuronal interactions and inhibit inflammatory cell activation [37]. The electrosprayed CNT/P(VDF-TrFE) interlayer exhibits a porous architecture that promotes the structural integrity of the FBI by creating mechanical interlocking between the hydrogel substrate and the ferroelectric layer (Figure S1).

By harnessing the differential swelling behaviors of the Alg-NHS and chitosan hydrogel layers within the bilayer hydrogel substrate, the FBI undergoes spontaneous morphing upon spraying with water, dynamically adjusting its curvatures from 0 to ~2.5 mm^{-1}, with the final curved configuration closely matching the geometry of fine peripheral nerves (Figure 2D,E; Video S1) [43–46]. Such self-rolling functionality confers active geometric compliance to fine and high-curvature peripheral nerves, enabling precise conformal contact and effectively addressing the geometric mismatch commonly confronted by traditional planar or cuff electrodes [15, 47–49]. In addition, intermolecular interactions via hydrogen and covalent bonds between the functional moieties of Alg-NHS and the abundant amino groups in biological tissues, allow the FBI to form robust interfacial adhesion with nerves upon contact, thereby achieving stable fixation after self-conforming to the target nerve bundles (Figure 2F) [42]. The shear strength for these bioadhesive interfaces reaches ~50 kPa (Figure 2G), comparable to that of the magnitude of commercial bio-glues [50]. Notably, such bioadhesive interface exhibits excellent biocompatibility (Figure S2), eliminating common biosafety concerns associated with commercial products [50].

Beyond self-rolling and interfacial adhesion, the FBI further demonstrates the unique functionality of generating electrical signals induced by polarization changes, analogous to those in natural neurons. Upon exposure to NIR light, the CNT-incorporated interlayer can convert light to heat, subsequently inducing the P(VDF-TrFE) dipole re-orientation in the upper film. Such dipole re-orientation can trigger reversible polarization changes and consequently the generation of electrical signals, mimicking the generation of action potentials that arise from ion-channel-mediated dynamics in natural neurons (Figure 2H; Figure S3) [37]. Notably, in comparison with the poled control films that CNTs are directly blended into the

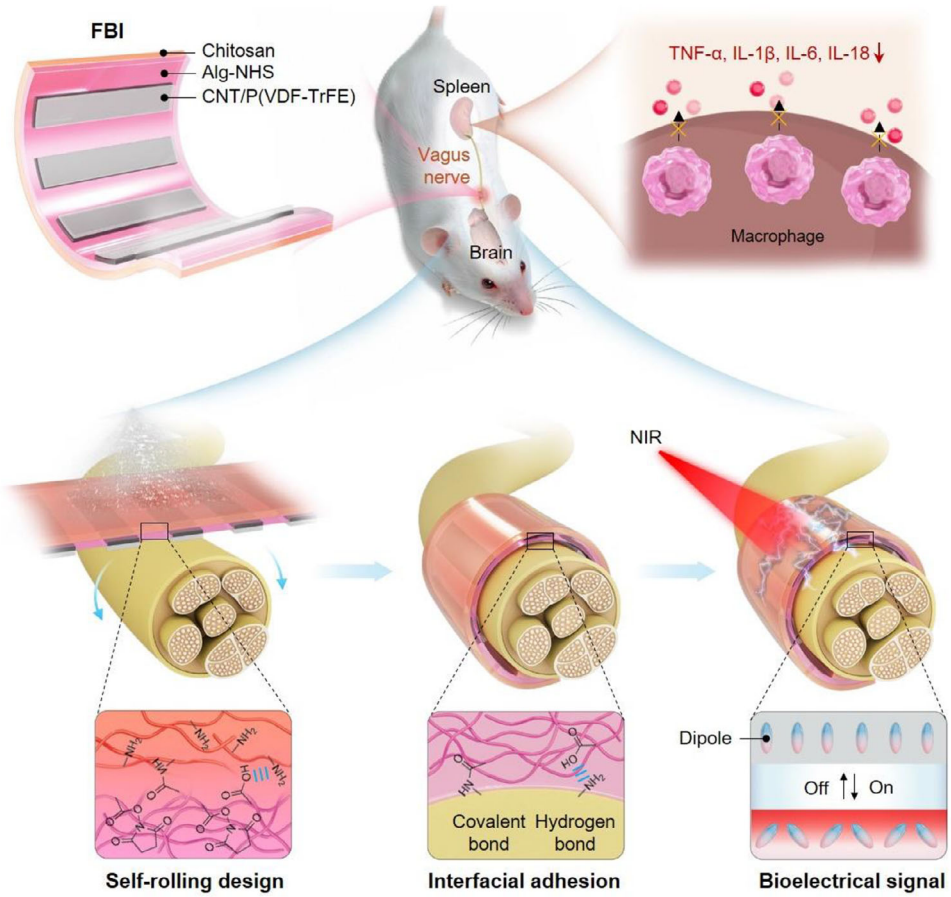

FIGURE 1 | Design of multifunctional ferroelectric bioelectronic interface (FBI). The FBI integrates ferroelectric poly(vinylidene fluoride-*co*-trifluoro ethylene) (P(VDF-TrFE)) polymer, photothermal carbon nanotubes (CNT), and bilayer natural polymer-based hydrogel (chitosan bottom layer + calcium-ion-crosslinked, NHS-ester-functionalized alginate (Alg-NHS) top layer). Upon sutureless implantation onto vagus nerves, the FBI provides NIR-mediated neuromodulation that suppresses the generation of pro-inflammatory cytokines (tumor necrosis factor (TNF)-α, interleukin (IL)-1β, IL-6, IL-18). Three synergistic functions are combined: (1) water-triggered self-rolling for actively geometric compliance with fine vagal fibers; (2) strong interfacial adhesion enabling sutureless fixation; and (3) NIR-driven, neuron-mimetic polarization-change bioelectrical signal for effective neuromodulation.

P(VDF-TrFE) matrix, the FBI featuring spatially separated CNT and P(VDF-TrFE) dipoles in distinct layers exhibits a higher ratio of ferroelectric β-phase and delivers ~50% higher electric outputs under identical NIR conditions (Figure 2H; Figure S4). Direct blending CNT disrupts the ferroelectric properties of P(VDF-TrFE) by altering its crystalline phase content and the crystalline domain size [51]. Moreover, the polarization changes of the FBI can be facilely tuned by varying the CNT mass ratio or NIR power density. The optimized mass ratio of CNT within the FBI is 4.0 wt%, which is determined based on the maximized peak-to-peak open-circuit voltage under short-pulse NIR irradiation (Figure 2I), whereas further increasing the CNT contents leads to unstable electrospraying jetting due to excessive conductivity [52]. Under the optimal CNT mass ratios, the peak-to-peak open-circuit voltage generated by the FBI can further be tuned, ranging from approximately 16 to 30 V by adjusting the NIR power density (Figure 2J). Together, these features endow the FBI with an unprecedented functional synergy of precise geometric matching, robust interfacial adhesion, and neuron-mimetic polarization change-induced bioelectrical signals, establishing a robust foundation for adaptive neural interfacing.

2.2 | Adaptive Communication with Cells

As an essential prerequisite of adaptive interfacing with nerves, the FBI must safely and effectively communicate with target cells [9]. To assess this, we cultured commonly used neuron-like rat phaeochromocytoma (PC12) cells onto the FBI and then applied pulsed 808 nm NIR irradiation at 15 mW·mm^{-2}, 1 Hz, and 20% duty cycle (Figure 3A), which enables deep tissue penetration and minimizes unsafe heat accumulation according to our previous study [53]. Intracellular Ca^{2+} imaging revealed that the PC12 cells were effectively excited by the FBI under such NIR irradiation, as indicated by significantly elevated fluorescence (Figure 3B; Video S2). Notably, the response of PC12 cells evoked by the FBI resembled the electrophysiological response of natural neurons in native neural networks, exhibiting intensity-dependent patterns [54]. As the NIR power density increased from 5 to 10 mW·mm^{-2}, intracellular Ca^{2+} fluorescence signals and cellular excitability increased correspondingly, whereas a further increase from 10 to 15 mW·mm^{-2} did not change the proportion of responding cells (Figure 3C–G; Videos S3 and S4), consistent with the excitability characteristics of natural neurons [55]. Under the

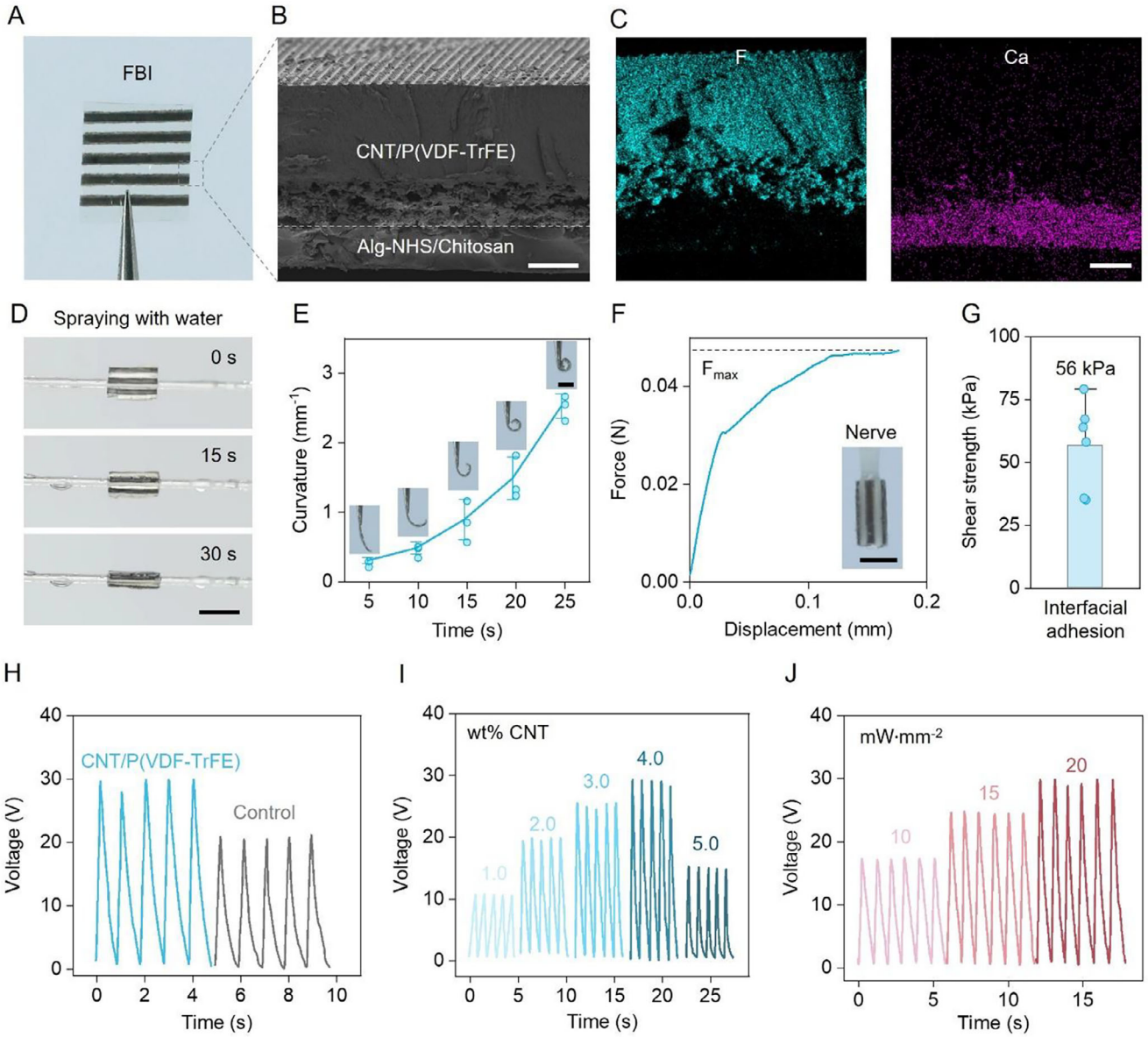

FIGURE 2 | Multiple functionalities of the FBI. (A) A representative macroscopic picture of the FBI in its original form of flattened film. The ferroelectric CNT/P(VDF-TrFE) stripes are periodically arranged onto the hydrogel substrate. (B) A representative cross-sectional picture of the FBI with hierarchical multilayer structures. The upper P(VDF-TrFE) film and the bottom hydrogel substrate are integrated by the porous electrosprayed CNT/P(VDF-TrFE) interlayer, which forms mechanical interlocking between different layers. Scale bar: 50 μm. (C) Distribution of the F and Ca elements within the FBI, indicative of the P(VDF-TrFE) and Alg-NHS hydrogel, respectively. Scale bar: 50 μm. (D) Time-lapse pictures of the FBI under spraying with water. Water induces differential swelling of the bilayer hydrogel, therefore driving self-rolling along a glass tube with a diameter of ~0.5 mm, mimicking fine vagus nerves. Scale bar: 5 mm. (E) The curvature changes of the FBI over time under the spraying with water. The insets exhibit corresponding shapes of the FBI at different times. Scale bar: 500 mm. (F) A representative curve for the bioadhesive interfaces between the FBI and a segment of ex vivo rat's vagus nerve in the lap-shear test for measuring shear strength. The left inset shows the interfacial adhesion between the FBI and a nerve segment. Scale bar: 1 mm. (G) Shear stress for the bioadhesive interfaces between the FBI and a segment of ex vivo rat's vagus nerve. $N = 6$ separate measurements. (H) Open-circuit voltages generated by the FBI and CNT-blended film under the identical NIR conditions (power density: 20 mW·mm^{-2}, 1 Hz frequency, 20% duty cycle). (I) Open-circuit voltages generated by the FBI containing different CNT contents (1, 2, 3, 4, or 5 wt% with respective to the mass of P(VDF-TrFE)) under the identical NIR conditions (power density: 20 mW·mm^{-2}, 1 Hz frequency, 20% duty cycle). (J) Open-circuit voltages generated by the FBI containing the identical CNT contents (4 wt% with respective to the mass of P(VDF-TrFE)) under the NIR irradiation with different power densities (power density: 10, 15, or 20 mW·mm^{-2}, 1 Hz frequency, 20% duty cycle).

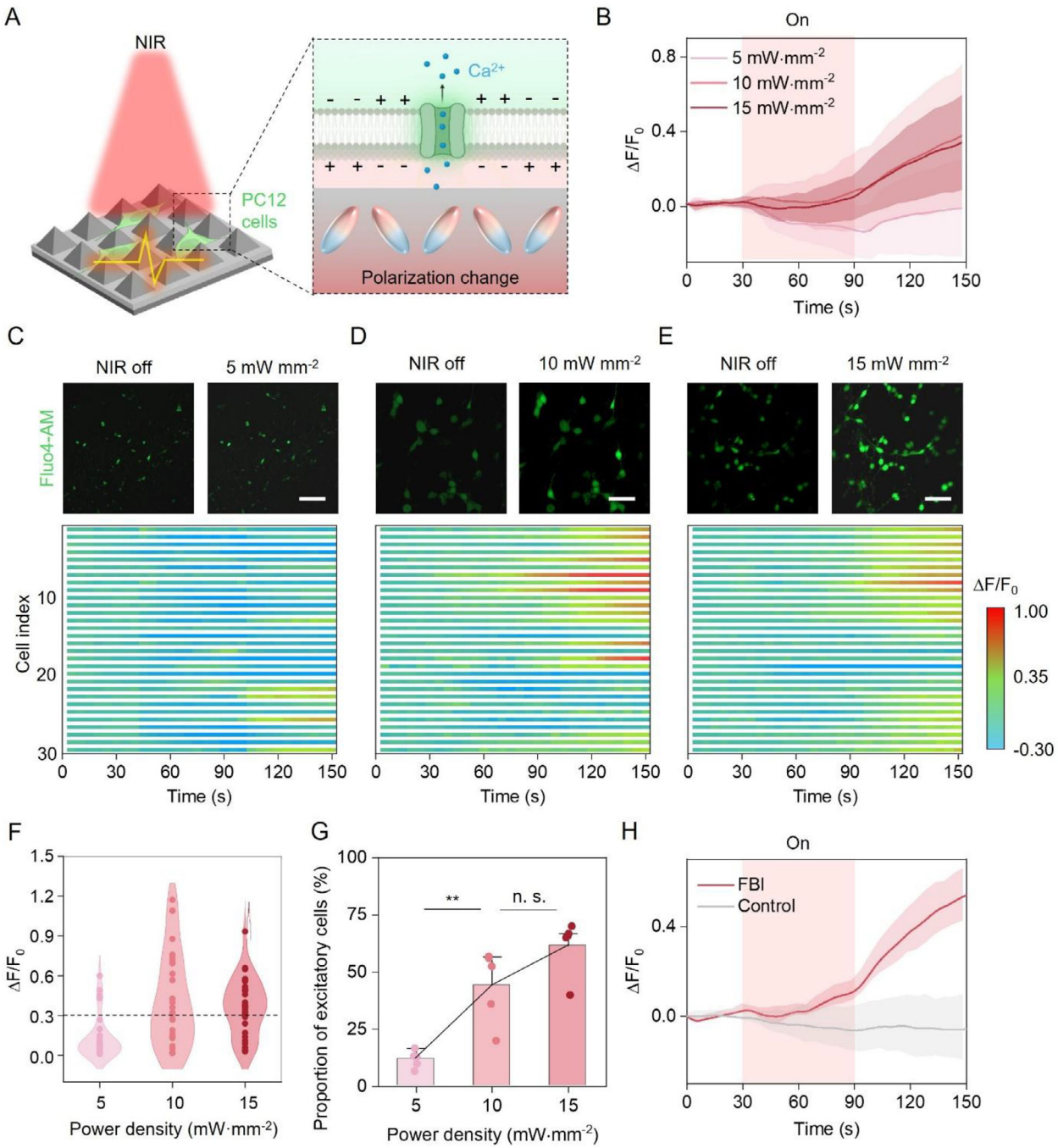

FIGURE 3 | Adaptive communication with cells. (A) Experimental scheme of monitoring cellular excitation by the FBI through intracellular Ca^{2+} imaging. The FBI generates bioelectrical signals under NIR irradiation due to NIR-induced polarization change, thereby modulating cellular membrane potential and subsequently evoking the opening of voltage-gated ion channels, inducing Ca^{2+} influx. (B) Average normalized fluorescence changes ($\Delta F/F_0$) over time for the PC12 cells stained with Fluo4 AM staining on the FBI under NIR irradiation (60 s duration, 1 Hz frequency, and 20% duty cycle) with different power densities (5, 10, or 15 mW·mm^{-2}). $N = 30$ cells. (C-E) Representative time-lapse fluorescence images and normalized fluorescence changes ($\Delta F/F_0$) over time for each PC12 cell stained with Fluo-4 AM staining on the FBI under NIR irradiation with different power densities (5, 10, or 15 mW·mm^{-2}). $N = 30$ cells in each group. Scale bars: 100 μm. (F) Statistics of peak values of normalized fluorescence change ($\Delta F/F_0$) for each PC12 cell cultured on the FBI under NIR irradiation (60 s duration, 1 Hz frequency, and 20% duty cycle) with different power densities (5, 10, or 15 mW·mm^{-2}). Cells with the normalized fluorescence change ($\Delta F/F_0$) above 30% are regarded excitatory. $N = 30$ cells in each group. (G) Statistics of the proportion of excitatory cells on the FBI under NIR irradiation with different power densities (5, 10, or 15 mW·mm^{-2}). $N = 5$ separate experiments. 5 mW·mm^{-2} versus 10 mW·mm^{-2}: $p = 0.009$; 5 mW·mm^{-2} versus 10 mW·mm^{-2}: $p = 0.093$. (H) Average normalized fluorescence changes ($\Delta F/F_0$) over time for the PC12 cells stained with Fluo4 AM staining on the FBI or the control films (Control, polyvinyl chloride-based films containing the identical CNT contents to the CNT/P(VDF-TrFE) films, exhibiting comparable photothermal effects to the CNT/P(VDF-TrFE) films but none of photo-pyroelectrical response, CNT/PVC) under the identical NIR conditions (power density: 15 mW·mm^{-2}, 1 Hz frequency, and 20% duty cycle). $N = 30$ cells. Statistical analyses into the data shown in G were performed using one-way ANOVA with two-tailed Student's *t*-test.

optimized NIR irradiation (15 mW·mm^{-2}, 1 Hz, and 20% duty cycle), approximately 60% of cells are reliably exited (Figure 3G). In contrast, control films with solely photothermal effects, yet the absence of NIR-induced polarization-change capability, cannot evoke cellular excitation under the identical NIR conditions (Figure 3H; Figure S5 and Video S5). These results validate that the FBI can activate ion channels via its unique capability of generating polarization change-induced bioelectrical signals like natural neurons, thereby triggering the polarization changes of cellular membranes and then cellular excitation [56]. Importantly, the neuron-like bioelectrical signals are delivered to target cells through photocapacitive effects, with negligible cytotoxic photo-electrochemical side reactions that commonly occur in existing optoelectronic materials [57]. As evidenced by intracellular monitoring, the generation of reactive oxygen species for the FBI is ~16-fold lower than that for photovoltaic silicon photodiodes under the identical NIR conditions (Figure S6) [37]. Accordingly, except at an evaluated NIR power density of 20 mW·mm^{-2} that leads to over-accumulation of heat, cell viability exhibits no statistically significant difference among conditions when NIR power density is gradually increased to 15 mW·mm^{-2} and the non-irradiated control (>99%, $p > 0.05$) for even consecutive 5 days of NIR irradiation (Figure S7). Numerical modeling further indicates that NIR irradiation at 15 mW·mm^{-2} can deliver light intensity with a magnitude of milliwatts per mm^2 through biological skin tissues with a depth of 10 mm, corresponding to generating an electrical field with a strength of around 5.0 V, adapted from vagus nerve stimulation even for large animals and humans (Figure S8). Collectively, these results demonstrate that the FBI can safely and effectively communicate with target cells, which are essential for in vivo neuromodulation.

2.3 | Seamless Interfacing with Vagus Nerve

We next evaluate the adaptability of the FBI at the vagus nerve interface and its in vivo neuromodulation efficacy in attenuating pro-inflammatory cytokine release using a rodent model of autoimmune disease (Figure 4A). To establish this model, lipopolysaccharide is intravenously injected to ignite systemic inflammation that imitates a representative autoimmune disease, i.e., endotoxemia [58]. As shown in Figure 4B and Video S6, the FBI can be facilely implanted onto the target vagus nerves of rats through the self-rolling-assisted active compliance and interfacial-adhesion-assisted sutureless fixation, thereby eliminating complicated operation, geometric mismatch, and tissue damage involved in the surgical implantation of conventional metallic cuff electrodes [18]. Micro-CT imaging confirms that the FBI realizes precise conformal contact with vagus nerve without evidence of nerve compression (Figure 4C). In contrast, implantation of flat control devices that lack self-rolling and interfacial adhesion functionalities leads to partial detachment and pronounced nerve compression, which can impair normal nerve function and compromise neuromodulation efficacy (Figure S9).

Following sutureless implantation with conform, seamless contact, the FBI is irradiated with NIR light to modulate the activity of the efferent vagus nerve, which is anticipated to attenuate the production of pro-inflammatory cytokines (e.g., TNF-α, IL-1β, IL-6, and IL-18). This approach leverages the established mechanism whereby stimulation of efferent vagus nerve endings in the spleen can indirectly promote acetylcholine release, thereby activating Janus kinase 2/Signal transducer and activator of transcription 3 (JAK2/STAT3)-mediated signaling cascades and inhibiting nuclear translocation of nuclear factor kappa-B (NF-κB) [17, 59]. Under the NIR irradiation with a pulse width of 200 ms, the implanted FBI undergoes a temperature rise of ~0.5 K, sufficient to induce bioelectrical signals while remaining biosafe for nerve tissues (Figure S10) [60]. Accordingly, we observe the upregulation of phosphorylated STAT3 and downregulation of phosphorylated p65, hallmarks of JAK2-STAT3 and NF-κB signaling pathways, respectively (Figure 4D–F; Figure S11) [61]. These results indicate that the implanted FBI effectively mediates the anti-inflammatory-related signaling pathways. Furthermore, we monitor the concentrations of pro-inflammatory cytokines (TNF-α, IL-1β, IL-6, and IL-18) in serum via enzyme-linked immunosorbent assay (ELISA). Remarkably, the FBI stimulation remotely controlled by NIR light can significantly decrease the concentrations of all these four types of pro-inflammatory cytokines in serum (Figure 4G–J; Figure S12). Consistent with the former in vitro cellular response, the anti-inflammatory effects of the FBI can also be tuned with NIR power density, realizing adjustable attenuations of pro-inflammatory cytokines (Figure S13). By integrating the synergistic functions, the FBI achieves seamless interfacing with the vagus nerve and enables effective, wireless, battery-free modulation of the vagus nerve activities.

2.4 | Long-Term Biosafety and Efficacy

Finally, we evaluate the long-term biosafety and reliability of the FBI in freely moving rats (Figure 5A). After the long-term implantation for 60 days, the FBI demonstrates no decay in generating polarization change-induced electrical signals under NIR irradiation (Figure S14). Throughout this period, the rats implanted with the FBI maintain normal motor functions (Video S7), and neither infection nor lesions are observed in vital organs (Figure S15). Moreover, there is no severe focal inflammation after the long-term implantation of the FBI, as revealed by minimal lymphocyte aggregation that correlates to inflammatory areas on the implantation sites, which is comparable to that of the sham-operated controls yet significantly lower than that implanted with flat control devices (Figure 5B,C). The FBI also demonstrates no sign of compression on the vagus nerve after the long-term implantation (Figure 5C). The immunofluorescence of Tuj-1, S100β, and CD68 for identifying neurons, Schwann cells, and macrophages/monocytes, respectively, further validates a negligible foreign body response to the FBI, which exhibits comparable expressions of all these biomarkers to the sham-operated controls (Figure 5D; Figure S16). In contrast, long-term implantation of flat control devices causes significant inflammation and foreign body responses, as evidenced by elevated CD68 expression, which may lead to detachment from nerve bundles and reduced neuromodulation efficacy (Figure 5E) [30].

In addition to the superior long-term biosafety, the FBI also demonstrates durable reliability in VNS for attenuating pro-inflammatory cytokines (TNF-α, IL-1β, IL-6, and IL-18). After

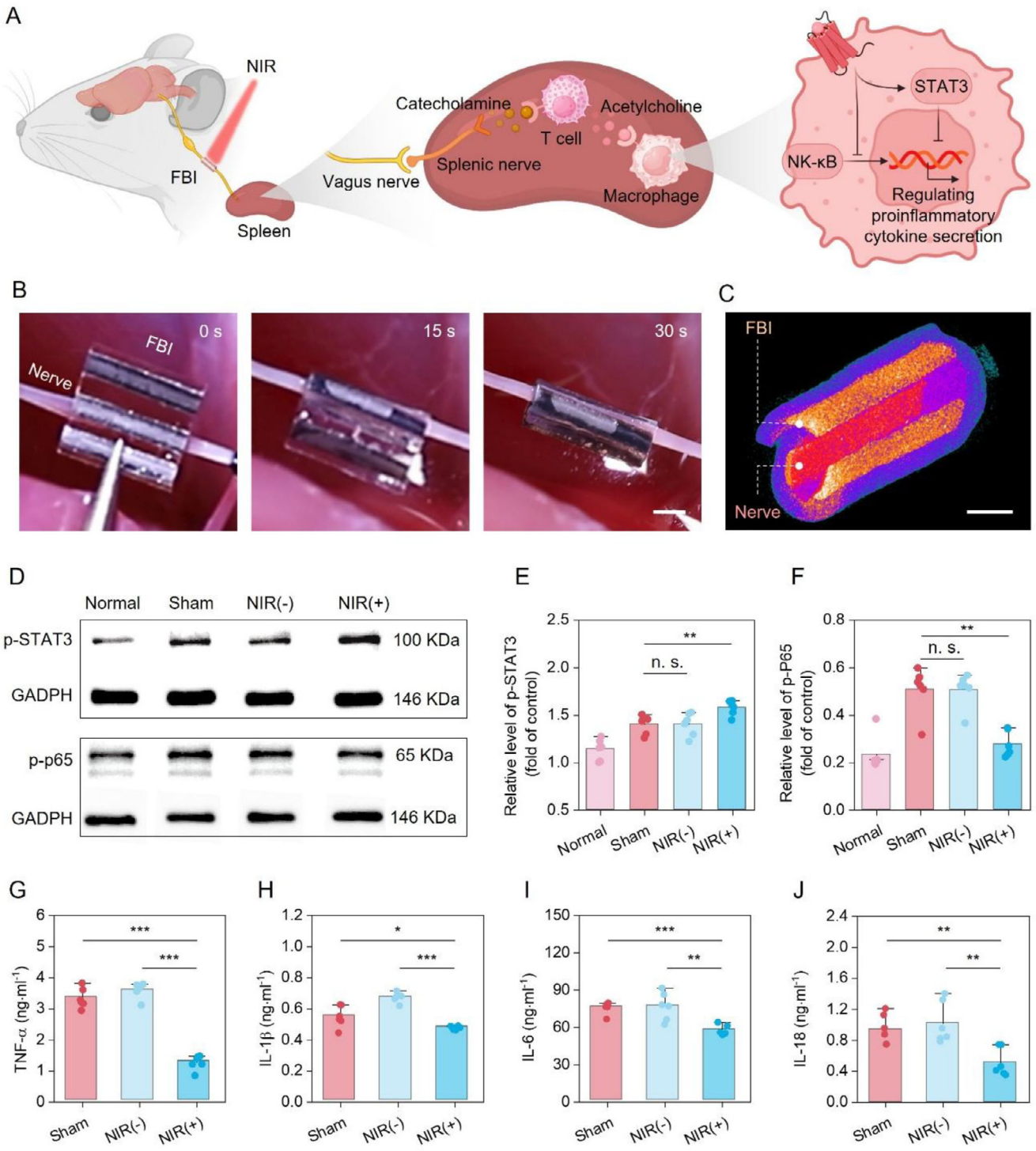

FIGURE 4 | Seamless interfacing with vagus nerve. (A) Sutureless implantation of the FBI for VNS and anti-inflammatory treatment. The FBI is implanted onto vagus nerves of rats, which can modulate vagus nerve activities under NIR irradiation, thereby activating the acetylcholine-related pathways in the spleen and inhibiting the production of pro-inflammatory cytokines by macrophages. (B) Time-lapse pictures demonstrating the implantation of the FBI onto the rat's vagus nerve. The FBI self-rolls under the spraying of sterilized water, wrapping the vagus nerve, and then self-closing via interfacial adhesion, without the requirement of additional suturing or mechanical locking. Scale bar: 1 mm. (C) A representative micro-CT image of the rat's vagus nerve implanted with the FBI, demonstrating conformal contact between the nerves and the FBI. Scale bar: 1 mm. (D) Agarose gel electrophoresis analysis of characteristic proteins (p-STAT3 and p-p65) for the cells collected from the extracted spleen tissues of rats. Normal: subjects implanted with the FBI and then intravenously injected with saline via femoral vein, without lipopolysaccharide (LPS) injection or NIR irradiation in the following treatments; Sham: subjects treated with sham surgery and then intravenously injected with LPS, with NIR irradiation in the following treatment; NIR(−): subjects implanted with the FBI and then intravenously injected with LPS, without NIR irradiation in the following treatment; and NIR(+): subjects implanted with the FBI and then intravenously injected with LPS, with NIR irradiation in the following treatment. (E,F) Relative levels of p-STAT3 (E) and p-p65 (F) proteins among different groups. p-STAT3: NIR(−) versus Sham $p = 0.988$, NIR(+) versus NIR(−) $p = 0.008$, $N = 6$ separate

60-day implantation, its anti-inflammatory efficacy shows no statistically significant difference compared with the initially implanted conditions (Figure 5F–I; Figure S17). By contrast, flat control devices that fail to adaptively interface with vagus nerves exhibit significantly decreased efficacy in inhibiting pro-inflammatory cytokines (Figure 5F). Notably, the vagus nerve is located near the skin, while the motion of subjects readily leads to displacement of vagus nerve bundles, leading to significant difficulties in forming adaptive interfaces for current implantable bioelectronics for VNS. Existing metallic, silicon photodiode-, and polymer-based modulators usually suffer from geometric mismatch, suture-related trauma, and substantial accumulation of cytotoxic reactive oxygen species. By contrast, the FBI with functional synergy of self-rolling, interfacial adhesion, and neuron-like bioelectrical signals enables long-term, biosafe, and reliable vagus nerve modulation, with superior stability and unprecedented persistent neuromodulation efficacy in freely moving animals, which are highly promising for translational applications (Figure 5G) [8, 12, 26, 28, 35, 36].

3 | Conclusions

In summary, we report an FBI composed of a bilayer natural polymer-based hydrogel, ferroelectric P(VDF-TrFE), and CNT, achieving unprecedented functional synergy: water-triggered self-rolling for precise geometric matching, robust interfacial adhesion that eliminates the need for sutures, and neuron-like bioelectrical signals driven by polarization change for adaptive communication with target cells. These integrated functions enable conformal, sutureless interfacing with fine, fragile vagus nerves and effective NIR-mediated neuromodulation, resulting in downregulation of multiple pro-inflammatory cytokines, including TNF-α, IL-1β, IL-6, and IL-18. Compared with conventional vagus nerve modulators, the FBI demonstrates superior long-term biosafety and reliability, characterized by no nerve compression, negligible focal inflammation, and sustained efficacy over 60 days of implantation. By providing durable and biosafe peripheral nerve modulation, the FBI represents a significant advance in implantable bioelectronics with great translational potential for refractory autoimmune diseases, while also holding great promise across diverse biomedical applications, including neurological disorder treatment and tissue engineering [62–64].

4 | Experimental Section

4.1 | Approval for Experiments with Animals

All the experiments involving animals were performed under the approval by the Animal Use and Care Committee of the Shenzhen Institute of Advanced Technology, Chinese Academy of Sciences with the project license (SIAT-IACUC-210301-TGS-ZQL-A1667-01) following ethical review.

4.2 | Fabrication of FBI

FBI was fabricated via stepwise procedures. First, the ferroelectric CNT/P(VDF-TrFE) layer was fabricated via casting and electrospraying according to our previous studies [65–68]. Briefly, P(VDF-TrFE) (Mw: 520 000–860 000, VDF:TrFE molar ratio = 70:30, Piezotech) was dissolved in dimethyl sulfoxide (DMSO, Aladdin) to formulate a solution with a concentration of 10 w/v%, which was poured into a 6-inch silicon mold featuring a micro-pyramid array (depth: 3.5 μm, width: 5.0 μm, pitch: 10.0 μm), dried at 80°C under ambient pressure overnight, and subsequently annealed at 130°C under vacuum for 6 h. The films were peeled off and corona-poled at 22 kV for 25 min. For comparative studies, PVC (*K*-value: 62-60, Aladdin) films and CNT-blended P(VDF-TrFE) films were fabricated using the above-described methods. Second, CNT/P(VDF-TrFE) microparticles were formed by electrospraying at 15 kV, with a nozzle-to-drum distance of 5 cm and a flow rate of 1.5 $mL{\cdot}h^{-1}$, which were deposited onto the underside of the P(VDF-TrFE) films. The contents of the CNT were varied from 1.0, 2.0, 3.0, 4.0, to 5.0 wt% with respect to the mass of P(VDF-TrFE). After electrospraying, the composite films were dried at 60°C for 2 h to remove residual solvents. Third, the Alg-NHS hydrogel layer was formed. Specifically. the CNT/P(VDF-TrFE) composite film was cut into stripe arrays (with a width of 0.5 mm and an edge-to-edge distance of 0.5 mm) by using a pre-machined mold and fixed onto a 2 cm × 6 cm glass slide. A precursor containing 5 w/v% sodium alginate (Sigma–Aldrich), 0.2 w/v% NHS (Sigma–Aldrich), 0.2 w/v% *N*-(3-dimethylaminopropyl)-*N′*-ethylcarbodiimide hydrochloride crystalline (EDC, Sigma–Aldrich) was added into the electrosprayed CNT-blended P(VDF-TrFE) layer, followed by air drying and ion crosslinking by immersing into a 1 M $CaCl_2$ solution. Fourth and finally, the chitosan hydrogel layer was fabricated by adding a chitosan solution (2% w/v in 2% v/v acetic acid) onto the Alg-NHS hydrogel layer, removing additional acetic acid by immersing it in a $NaHCO_3$ aqueous solution, and air drying at room temperature for 10 h, resulting in FBI. The as-prepared FBI was sealed and stored at room temperature.

4.3 | Characterizations

The morphologies of FBI samples were characterized under a field-emission scanning electron microscope (SEM, Sigma 300, Zeiss). For the SEM characterizations, we broke the samples in liquid nitrogen and coated the films with a thin layer of Au via sputtering. Both top-view and cross-sectional images of the samples were recorded. The distributions of elements, F (for identifying P(VDF-TrFE)) and Ca (for identifying Alg-NHS) were

experiments. p-p65: NIR(+) versus Sham $p = 0.986$, NIR(+) versus NIR(−) $p = 0.001$, $N = 6$ separate experiments. (G-J) Concentrations of tumor necrosis factor (TNF, G), interleukin (IL)-1β (H), IL-6 (I), and IL-16 (J) in serum collected 4 h later after NIR irradiation among different groups. TNF-α: NIR(+) versus Sham $p < 0.001$, NIR(+) versus NIR(−) $p < 0.001$, $N = 6$ separate experiments. IL-1β: NIR(+) versus Sham $p = 0.045$, NIR(+) versus NIR(−) $p < 0.001$, $N = 6$ separate experiments. IL-6: NIR(+) versus Sham $p < 0.001$, NIR(+) versus NIR(−) $p = 0.006$, $N = 6$ separate experiments. IL-18: NIR(+) versus Sham $p = 0.003$, NIR(+) versus NIR(−) $p = 0.004$, $N = 6$ separate experiments. Statistical analyses into the data shown in E-J were performed using one-way ANOVA with two-tailed Student's *t*-test.

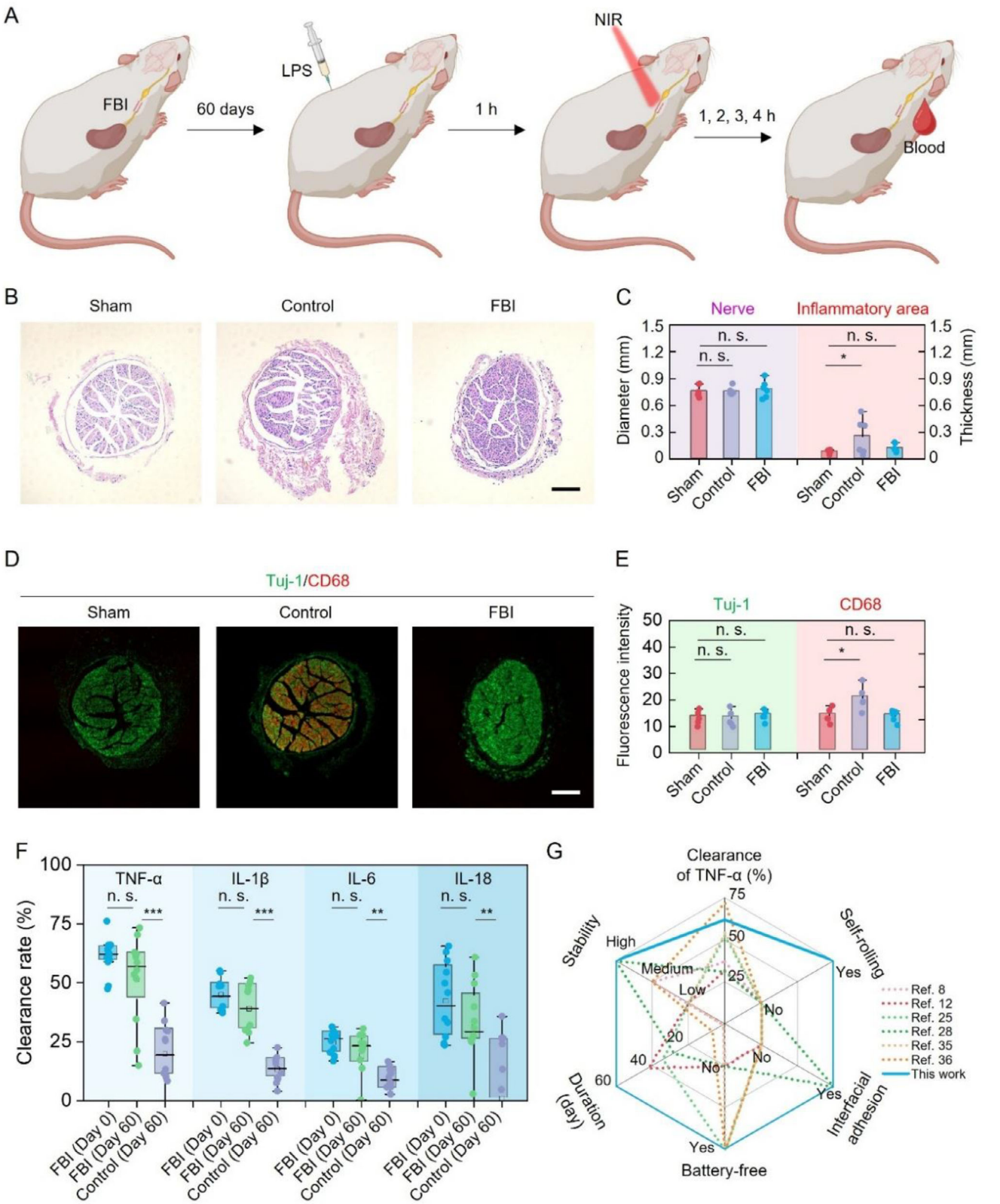

FIGURE 5 | Long-term biosafety and reliability. (A) Experimental scheme for assessing long-term biosafety and reliability. The rats are implanted with the FBI for 60 days and then injected with LPS for eliciting inflammation. NIR irradiation is subsequently performed, followed by the collection of serum at different time points (1, 2, 3, and 4 h later). (B) Representative histological images of vagus nerves at the implantation sites after 60-day implantation. Sham: subjects treated with sham surgery and then housed for 60 days; Control: subjects implanted with flat control devices (i.e., flat CNT/P(VDF-TrFE) films without the hydrogel substrate) for 60 days; and FBI: subjects with implanted the FBI for 60 days. Scale bar: 250 μm. (C) Statistics of vagus nerve diameters and inflammatory area thickness for the tissues at the implantation sites at post-operative day 60. Nerve diameter: Control versus Sham $p = 0.960$, FBI versus Sham $p = 0.662$, $N = 6$ separate experiments. Inflammatory area thickness: Control versus Sham $p = 0.047$,

mapped using an energy dispersive X-ray spectroscope (EDS, XFlash 6|60 detector, Bruker). The macroscopic pictures of the samples (at static or morphing conditions) were recorded by a digital camera (EOS 7D Mark II, Canon). Fourier Transform infrared spectroscopic (FTIR) characterizations were also performed to assess the fraction of β phase ($F(\beta)$) of the P(VDF-TrFE) within the samples, which was calculated according to the Beer-Lambert law using the following Equation (1):

$$F(\beta) = A_\beta / \left(1.26\, A_\alpha + A_\beta\right) \times 100\% \quad (1)$$

where A_α and A_β represent the characteristic absorption peaks to the α-phase (764 cm^{-1}) and β-phase (843 cm^{-1}) of the P(VDF-TrFE), respectively.

The temperature changes of the samples under NIR irradiation in air were monitored using a high-resolution infrared thermometer (R550Pro, 21 μm, NEC). The samples were irradiated by pulsed NIR irradiation (φ: 10 mm, 20% duty cycle, frequency: 1 Hz) with varying power densities (10, 15, or 20 $mW{\cdot}mm^{-2}$) generated by an 808-nm NIR laser with a built-in digital shutter (Beijing Hong Optoelectric Co. Ltd.). The temperature changes of the samples under NIR irradiation in vivo were monitored using a T-type ultrafine thermocouple (KPS-T-0.05-1000-CZ, Kaipusen), which was inserted at the interface between the sample and the nerve.

To evaluate electrical properties, we coated FBI with 200-nm ITO layers (as transparent electrodes) via sputtering on both sides. Open-circuit voltages generated by the samples (square shapes with a width to length of 1.50 cm × 1.50 cm) under pulsed NIR irradiation (φ: 10 mm, 20% duty cycle, frequency: 1 Hz) were measured using a digital source meter (2470, Keithley). Using such methods, the electrical properties of samples containing different CNT contents (1, 2, 3, 4, or 5 wt%) and irradiated by NIR light with different power densities (10, 15, or 20 $mW{\cdot}mm^{-2}$) were evaluated. The electrical properties of FBI were also evaluated through scanning Kelvin probe microscopy (SKPM). Surface potential measurements were performed before implantation and after 60 days using an SKPM system (Asylum Research Cypher S, USA) under 808 nm near-infrared laser irradiation (power: 5 $mW{\cdot}mm^{-2}$, 20% duty cycle, frequency: 1 Hz). A local silver paste coating connected to ground was applied to maintain the initial surface potential of the composite film near zero. The changes in surface potential near the grounded regions of the CNT/P(VDF-TrFE) film under periodic NIR illumination (808 nm) were recorded at 2.5 min intervals at room temperature.

4.4 | Interfacial Adhesion Test

Fresh vagus nerves isolated from rats were used in the test. The dried FBI was placed in contact with the nerve, which was then sprayed with a small amount of water to induce self-rolling and wrapping around the nerve. The FBI and the nerve fiber were then clamped separately by a universal material testing machine to record the force and displacement under tensile. The maximum force (F_{max}) recorded was used to calculate the shear strength of the bioadhesive interface between the samples and the nerves according to the following Equation (2):

$$\text{Shear strength} = F_{max} / (\pi D \times L) \quad (2)$$

where D represents the outer diameter of the nerve fiber, and L is the overlapping length between FBI and the nerve.

4.5 | Cell Viability Assessment

PC12 cells, as a common neuronal model, were used in this investigation. We obtained PC12 cells from Procell Life Science & Technology Co., Ltd., China, then incubating them using Dulbecco's modified eagle medium (DMEM, Gibco) with supplemented 5 v/v% fetal bovine serum (FBS, ScienCell) and 1 v/v% penicillin/streptomycin solution (P/S, ScienCell) in an incubator (5 v/v% CO_2, 37°C, humid atmosphere, CLM-170B-B-NF, ESCO). After an above 70% confluence, the PC12 cells were trypsinized and seeded onto sterilized samples at a cell seeding density of 7000 $cells{\cdot}cm^{-2}$. Pulsed NIR irradiation (1 Hz, 20% duty cycle) was then daily performed for 10 min since day 1 post-seeding with power densities (0, 0.5, 1.0, 1.5, 2 W cm^{-2}). At specific time points (first, third, and fifth day), the PC12 cells were stained using a LIVE/DEAD Viability/Cytotoxicity kit (Invitrogen) according to the manufacturer's protocol. Fluorescence images were captured using a fluorescent microscope (Olympus X71). The acquired images were processed using the ImageJ software.

4.6 | Intracellular Ca^{2+} Imaging

PC12 cells were seeded on sterilized samples in a 96-well plate for 48 h. After 1-day cell culture, the cell-laden samples were washed with warm phosphate-buffered saline (PBS, Gibco), stained with Fluo-4 AM (Invitrogen) by using a staining solution prepared by mixing 100 μL DMEM with 1 μL dye stock solution (formulated by dissolving 50 μg Fluo-4 AM in 40 μL DMSO (Sigma–Aldrich) with an addition of 20 w/v% Pluronic F-127 (Sigma–Aldrich)) in

FBI versus Sham $p = 0.067$, $N = 6$ separate experiments. (D) Representative immunofluorescence images of vagus nerves at the implantation sites after 60-day implantation. Scale bar: 250 μm. (E) Statistics of relative fluorescence intensity for Tuj-1 and CD68 in the tissues at the implantation sites at post-operative day 60. Tuj-1: Control versus Sham $p = 0.443$, FBI versus Sham $p = 0.311$, $N = 5$ separate experiments. CD68: Control versus Sham $p = 0.043$, FBI versus Sham $p = 0.183$, $N = 5$ separate experiments. (F) Statistics of clearance percentages for TNF-α, IL-1β, IL-6, and IL-16 in serum with acute (Day 0) and long-term (Day 60) implantation of FBI or the long-term implantation of flat control devices (Control (Day 60)). TNF-α: FBI (Day 60) versus FBI (Day 0) $p = 0.525$, Control (Day 60) versus FBI (Day 60) $p < 0.001$, $N = 10$. IL-1β: FBI (Day 60) versus FBI (Day 0) $p = 0.167$, Control (Day 60) versus FBI (Day 60) $p < 0.001$, $N = 10$. IL-6: FBI (Day 60) versus FBI (Day 0) $p = 0.134$, Control (Day 60) versus FBI (Day 60) $p = 0.008$, $N = 12$. IL-18: FBI (Day 60) versus FBI (Day 0) $p = 0.128$, Control (Day 60) versus FBI (Day 60) $p = 0.003$, $N = 12$. (J) Comparison of the FBI with other reported implantable bioelectronics for VNS in terms of anti-inflammation efficacy, self-rolling, interfacial adhesion, battery-free neuromodulation, implantation duration, and stability [8, 12, 26, 28, 35, 36]. Statistical analyses into the data shown in C, E, and F were performed using one-way ANOVA with two-tailed Student's t-test.

dark at 37°C for 30 min, and then incubated with pre-warmed artificial cerebrospinal fluid (aCSF; containing 126 mM NaCl, 2.5 mM KCl, 2 mM $CaCl_2$, 2 mM $MgCl_2$, 1.25 mM NaH_2PO_4, 26 mM $NaHCO_3$, and 10 mM glucose, pH 7.4) in dark at 37°C for another 30 min. Afterwards, time-lapse fluorescence images were acquired using a confocal microscope (LSM 990, Zeiss) for 30 s before, 60 s during, and 60 s after NIR irradiation (1 Hz, 20% duty cycle, power densities: 0.5, 1.0, and 1.5 $W \cdot cm^{-2}$). The fluorescence intensity of each cell over time (F_i) was measured using ImageJ. The normalized fluorescence change ($\Delta F/F_0$) was calculated according to the following Equation (3):

$$\Delta F/F_0 = (F_i - F_0)/F_0 \quad (3)$$

where F_0 represents the initial fluorescence intensity during recording. The cells with the normalized fluorescence change beyond 30% were defined as excitatory.

4.7 | Animal Model and Surgery

Male Sprague-Dawley rats (450–500 g) were randomly divided into five groups: i) Normal: subjects intravenously injected with saline via femoral vein and then implanted with FBI, without NIR irradiation in the following treatment; ii) Sham: subjects intravenously injected with lipopolysaccharide (LPS, 10 mg/kg) via femoral vein and then treated with sham surgery, with NIR irradiation in the following treatment; iii) NIR(−): subjects intravenously injected with LPS via femoral vein and then implanted with FBI, without NIR irradiation in the following treatment; iv) NIR(+): subjects intravenously injected with LPS and then implanted with FBI, with NIR irradiation in the following treatment; and v) Control: subjects intravenously injected with LPS and then implanted with the flat control devices, with NIR irradiation in the following treatment.

During implantation, the rats were anesthetized with 4% isoflurane in oxygen, and then placed on a thermostatic surgical plate (37°C) to maintain core body temperature. A midline incision (about 2 cm) was made in the neck of rats. The subcutaneous tissue and sternocleidomastoid muscle were bluntly dissected to expose the right carotid sheath. The vagus nerve trunk (about 10 mm in length) was carefully isolated, avoiding damage to adjacent vessels. A sterilized sample (FBI or the flat film) with a typical size of 3 × 5 mm was placed onto the isolated vagus nerve, followed by the spraying of 2 mL of sterilized water to induce self-rolling around the nerve and the maintenance of ∼2 min to form a stable bioadhesive interface. The incision was then sutured, and the rats were fed under standard housing conditions. NIR irradiation was performed using the 808-nm NIR laser, using the parameters of 1 Hz, 20% duty cycle, and a power density of 1.5 $W \cdot cm^{-2}$. The laser beam with a spot diameter of ∼1 cm was irradiated toward the sites of implantation.

4.8 | ELISA Measurement

The concentrations of inflammatory cytokines (TNF-α, IL-1β, IL-6, and IL-18) in the serum of subjects were quantified through ELISA. Briefly, Blood samples (1 mL for each subject) were collected from the left carotid artery using a 22 G needle at 1, 2, 3, and 4 h after NIR irradiation, which were then placed in gel-separator tubes, for 10 min at room temperature, and centrifuged at 3500 rpm for 15 min. Serum was aliquoted and stored at −20°C until analysis. During ELISA measurement, serum samples were thawed at room temperature for 60 min, then analyzed using corresponding ELISA kits (TNF-α: R&D Systems Cat# Val 902, IL-1β: R&D Systems Cat# Val 903, IL-6: R&D Systems Cat# Val 901, and IL-18: R&D Systems Cat# Val 904) according to the manufacturer's protocol. A four-parameter logistic (4-PL) curve was used to determine cytokine concentrations from absorbance values, which were then multiplied by appropriate dilution factors to obtain final concentrations.

4.9 | Western Blot Analysis

The spleen was dissected from euthanized subjects, rinsed with cold PBS three times to remove residual blood and connective tissue, minced into ∼1 mm^3 pieces, and then treated with cold RIPA lysis buffer (containing 1× protease inhibitor cocktail and 1 mM phenylmethanesulfonyl fluoride). The as-treated tissue was incubated on ice for 20 min and transferred to a pre-chilled grinding tube for homogenization using a tissue homogenizer (30 Hz, 30-s on, 10-s off, 10-min duration, 4°C). The lysate was centrifuged at 14 000 rpm for 15 min at 4°C. The supernatant was then collected as the total protein extract. Protein concentration was determined using a BCA assay kit (Thermo Scientific), and samples were adjusted to a uniform concentration (e.g., 3 $\mu g \cdot \mu L^{-1}$) with lysis buffer. For immunoblotting, proteins were separated by SDS-PAGE under constant voltage (80 V in the stacking gel, 120 V in the separation gel) until the dye front reached the bottom. Proteins were transferred to a methanol-activated PVDF membrane using a wet transfer system (200 mA, 90 min). The membrane was blocked with 5% non-fat milk in Tris-borate-sodium Tween-20 buffer (TBST) for 1 h at room temperature, then incubated with primary antibodies (p-STAT3: Abcam, ab267373, 1:10 000; p-p65: Abcam, ab53489, 1:10 000) at 4°C overnight. After washing three times with TBST (10 min each), the membrane was incubated with an HRP-conjugated secondary antibody (1:5000) for 1 h at room temperature, washed three times, and treated with ECL substrate (Thermo Scientific). Chemiluminescent signals were captured using a gel imaging system, and band intensities were quantified with ImageJ.

4.10 | Micro-CT Imaging

Subjects implanted with the FBI or the flat films were euthanized. A segment of the vagus nerve (∼10 mm) with the implants was carefully dissected. The samples were fixed in 4% paraformaldehyde (4°C) for 12 h, followed by washing three times for 10 min with PBS. Afterwards, tissues were treated with 0.2% Triton X-100 in PBS at 4°C for 30 min and washed three times with PBS again. A dual-end gradient staining was subsequently performed. One terminal of the nerve was vertically immersed in iohexol solution (350 mg/mL), ensuring the implant remained above the liquid level, and incubated at 4°C for 24 h. Another terminal was then

stained under the same conditions after inverting the sample. After staining the tissue, the sample was rinsed with PBS, gently blotted dried, and then scanned using a high-resolution micro-CT system (SkyScan 1272, Shuyun Instrument). Reconstruction was performed with the accompanying NRecon software, and 3D visualization with pseudo-color r was carried out using the CTvox software.

4.11 | H&E Staining

After euthanasia, a segment of the vagus nerve (~10 mm) with the implants, as well as major organs (heart, liver, spleen, lung, kidney), were dissected, which were fixed in 4% paraformaldehyde (4°C) for 12 h, washed three times with PBS and water, dehydrated through a graded ethanol series, embedded in paraffin, and then cryosectioned into slices using a microtome. The slices were then deparaffinized in xylene and rehydrated through a descending ethanol gradient, followed bystaining with Harris hematoxylin for 8 min at room temperature, counterstained with 0.5% eosin (containing 0.1% glacial acetic acid) for 1 min, and mounted with neutral balsam. Images were acquired using a slide scanning system (Olympus VS200 Loader).

4.12 | Immunofluorescence

Tissue slices were first prepared according to the above-described procedures, which were then blocked with 5 w/v% bovine serum albumin (BSA, Sigma–Aldrich) in PBS with supplemented 0.1 w/v% Triton X-100 for 1 h at room temperature, incubated overnight at 4°C with a mixture of primary antibodies (i.e., Tuj1: Abcam, ab78078, 1:200, S100β: Abcam, ab52642, 1:500, and CD68: Abam, ab53444, 1:300), and then corresponding secondary antibodies for 1 h at 37°C (Tuj1: Invitrogen, Alexa Fluor 488-conjugated goat anti-mouse IgG (1:500), S100β: Invitrogen, Cy3-conjugated goat anti-rabbit IgG (1:600), and CD68: Invitrogen, Cy5-conjugated goat anti-rat IgG (1:600). Nuclei were stained with 4',6-diamidino-2-phenylindole (DAPI, Invitrogen, 1 μg/mL). Fluorescence images were acquired using the confocal microscope. Analyses of fluorescence intensity were performed using the ImageJ software.

4.13 | Numerical Modeling

Numerical modeling to simulate the NIR propagation through biological tissues was performed according to the established Monte Carlo modeling of light transport in tissues (MCML) [69], using open-source codes mcxyz.c (https://omlc.org/software/mc/mcxyz/index.html) that suits multi-tissue layers. The tissue model consisted of 2-mm epidermis and 8-mm dermis tissues. The parameters of NIR light irradiated to the tissues were set with a wavelength of 808 nm, a spot size of 10 mm, and a power density of 15 mW.mm^{-2}. The strength of electrical filed generated by the FBI under NIR irradiation was calculated according to the pyroelectric coefficient of the FBI (1.2×10^5 C·K^{-1}·m^{-2}) and the specific heat capability of human skin tissues (3.5 J·g^{-1}·K^{-1}). The output files were convolved and illustrated using the software MATLAB.

4.14 | Statistical Analysis

Data are presented as means ± standard error of mean (S. E. M.). We performed statistical analysis using one-way analysis of variance (ANOVA) and analyzed the probability value (P) through the two-tailed Student's *t*-test.

Author Contributions

X.D. conceived the idea and supervised the research. X.Z. and Q.Z. conducted the experiments. Q.Z. and X.D. analyzed the results and wrote the manuscript with the assistance of Y.W. All authors contributed to the discussion and interpretation of the results.

Acknowledgements

The authors acknowledge the financial support provided by the National Natural Science Foundation of China (52261160380, 52022102, and 52173148), the Shenzhen Medical Research Fund (B2302045), National Key R&D Program of China (2017YFA0701303), the Youth Innovation Promotion Association of CAS (Y2023100, 2022368), and the Fundamental Research Program of Shenzhen (RCJC20221008092729033, JCYJ20220818101800001).

Conflicts of Interest

The authors declare no conflicts of interest.

Data Availability Statement

The data that support the findings of this study are available from the corresponding author upon reasonable request.

References

1. N. Rossetti, W. Song, P. Schnepel, et al., "Control of Spatiotemporal Activation of Organ-specific Fibers in the Swine Vagus Nerve by Intermittent Interferential Current Stimulation," *Nature Communications* 16 (2025): 4419, https://doi.org/10.1038/s41467-025-59595-4.

2. V. A. Pavlov and K. J. Tracey, "Bioelectronic Medicine: Preclinical Insights and Clinical Advances," *Neuron* 110 (2022): 3627–3644, https://doi.org/10.1016/j.neuron.2022.09.003.

3. J. K. Krauss, N. Lipsman, T. Aziz, et al., "Technology of Deep Brain Stimulation: Current Status and Future Directions," *Nature Reviews Neurology* 17 (2021): 75–87, https://doi.org/10.1038/s41582-020-00426-z.

4. S. R. Patel and C. M. Lieber, "Precision Electronic Medicine in the Brain," *Nature Biotechnology* 37 (2019): 1007–1012, https://doi.org/10.1038/s41587-019-0234-8.

5. D. Fox, "The Shock Tactics Set to Shake up Immunology," *Nature* 545 (2017): 20–22, https://doi.org/10.1038/545020a.

6. M. A. Wheeler and F. J. Quintana, "The Neuroimmune Connectome in Health and Disease," *Nature* 638 (2025): 333–342, https://doi.org/10.1038/s41586-024-08474-x.

7. H. Jin, M. Li, E. Jeong, F. Castro-Martinez, and C. S. Zuker, "A Body–brain Circuit That Regulates Body Inflammatory Responses," *Nature* 630 (2024): 695–703, https://doi.org/10.1038/s41586-024-07469-y.

8. L. V. Borovikova, S. Ivanova, M. Zhang, et al., "Vagus Nerve Stimulation Attenuates the Systemic Inflammatory Response to Endotoxin," *Nature* 405 (2000): 458–462, https://doi.org/10.1038/35013070.

9. Y. Huang, K. Yao, Q. Zhang, et al., "Bioelectronics for Electrical Stimulation: Materials, Devices and Biomedical Applications," *Chemical Society Reviews* 53 (2024): 8632–8712, https://doi.org/10.1039/D4CS00413B.

10. E. M. Song, J. H. Li, S. M. Won, W. B. Bai, and J. A. Rogers, "Materials for Flexible Bioelectronic Systems as Chronic Neural Interfaces," *Nature Materials* 19 (2020): 590–603, https://doi.org/10.1038/s41563-020-0679-7.

11. A. S. Caravaca, A. L. Gallina, L. Tarnawski, et al., "Vagus Nerve Stimulation Promotes Resolution of Inflammation by a Mechanism That Involves Alox15 and Requires the α7nAChR Subunit," *Proceedings of the National Academy of Sciences* 119 (2022): 2023285119, https://doi.org/10.1073/pnas.2023285119.

12. F. A. Koopman, S. S. Chavan, S. Miljko, et al., "Vagus Nerve Stimulation Inhibits Cytokine Production and Attenuates Disease Severity in Rheumatoid Arthritis," *Proceedings of the National Academy of Sciences* 113 (2016): 8284–8289, https://doi.org/10.1073/pnas.1605635113.

13. A. Carnicer-Lombarte, A. J. Boys, A. Güemes, et al., "Ultraconformable Cuff Implants for Long-term Bidirectional Interfacing of Peripheral Nerves at Sub-nerve Resolutions," *Nature Communications* 15 (2024): 7523, https://doi.org/10.1038/s41467-024-51988-1.

14. G. Meneses, M. Bautista, A. Florentino, et al., "Electric Stimulation of the Vagus Nerve Reduced Mouse Neuroinflammation Induced by Lipopolysaccharide," *Journal of Inflammation* 13 (2016): 33, https://doi.org/10.1186/s12950-016-0140-5.

15. R. Feiner and T. Dvir, "Tissue–electronics Interfaces: from Implantable Devices to Engineered Tissues," *Nature Reviews Materials* 3 (2017): 17076, https://doi.org/10.1038/natrevmats.2017.76.

16. J. W. Salatino, K. A. Ludwig, T. D. Y. Kozai, and E. K. Purcell, "Glial Responses to Implanted Electrodes in the Brain," *Nature Biomedical Engineering* 1 (2017): 862–877, https://doi.org/10.1038/s41551-017-0154-1.

17. M. Rosas-Ballina, M. Ochani, W. R. Parrish, et al., "Splenic Nerve Is Required for Cholinergic Antiinflammatory Pathway Control of TNF in Endotoxemia," *Proceedings of the National Academy of Sciences* 105 (2008): 11008–11013, https://doi.org/10.1073/pnas.0803237105.

18. V. Geyfman, R. H. Storm, S. C. Lico, and J. W. Oren, "Cardiac Tamponade as Complication of Active-Fixation Atrial Lead Perforations: Proposed Mechanism and Management Algorithm," *Pacing and Clinical Electrophysiology* 30 (2007): 498–501, https://doi.org/10.1111/j.1540-8159.2007.00699.x.

19. Z. Zhao, G. D. Spyropoulos, C. Cea, J. N. Gelinas, and D. Khodagholy, "Ionic Communication for Implantable Bioelectronics," *Science Advances* 8 (2022): abm7851, https://doi.org/10.1126/sciadv.abm7851.

20. W. Chen, L. Zhai, S. Zhang, et al., "Cascade-heterogated Biphasic Gel Iontronics for Electronic-to-multi-ionic Signal Transmission," *Science* 382 (2023): 559–565, https://doi.org/10.1126/science.adg0059.

21. R. Dong, L. Wang, Z. Li, et al., "Stretchable, Self-Rolled, Microfluidic Electronics Enable Conformable Neural Interfaces of Brain and Vagus Neuromodulation," *ACS Nano* 18 (2024): 1702–1713, https://doi.org/10.1021/acsnano.3c10028.

22. C. Dong, A. Carnicer-Lombarte, F. Bonafè, et al., "Electrochemically Actuated Microelectrodes for Minimally Invasive Peripheral Nerve Interfaces," *Nature Materials* 23 (2024): 969–976, https://doi.org/10.1038/s41563-024-01886-0.

23. J. Yi, G. Zou, J. Huang, et al., "Water-responsive Supercontractile Polymer Films for Bioelectronic Interfaces," *Nature* 624 (2023): 295–302, https://doi.org/10.1038/s41586-023-06732-y.

24. Y. Liu, J. Li, S. Song, et al., "Morphing Electronics Enable Neuromodulation in Growing Tissue," *Nature Biotechnology* 38 (2020): 1031–1036, https://doi.org/10.1038/s41587-020-0495-2.

25. Y. C. Zhang, N. Zheng, Y. Cao, et al., *Science Advances* 5 (2019): aaw1066.

26. Q. Wang, M. Yang, R. Sun, et al., "A Biodegradable Capacitive-coupling Neurostimulator for Wireless Electroceutical Treatment of Inflammatory Bowel Diseases," *Science Advances* 11 (2025): adu5887.

27. S. An, T. Kim, J. Jang, et al., "Self-bondable and Strain-durable Electroceuticals Using Self-healing and Stretchable Conducting Nanocomposite Trilayer for Effective Vagus Nerve Stimulation," *ACS Nano* 19, no. 37 (2025): 33091–33102.

28. M. Yang, L. Wang, W. Liu, et al., "Highly-stable, Injectable, Conductive Hydrogel for Chronic Neuromodulation," *Nature Communications* 15 (2024): 7993, https://doi.org/10.1038/s41467-024-52418-y.

29. L. Qian, F. Jin, T. Li, et al., "Self-Adhesive and Self-Sustainable Bioelectronic Patch for Physiological Feedback Electronic Modulation of Soft Organs," *Advanced Materials* 36 (2024): 2406636, https://doi.org/10.1002/adma.202406636.

30. M. Yang, P. Chen, X. Qu, et al., "Robust Neural Interfaces with Photopatternable, Bioadhesive, and Highly Conductive Hydrogels for Stable Chronic Neuromodulation," *ACS Nano* 17, no. 2 (2023): 885–895.

31. M. Silvera Ejneby, M. Jakesova, J. J. Ferrero, et al., "Chronic Electrical Stimulation of Peripheral Nerves via Deep-red Light Transduced by an Implanted Organic Photocapacitor," *Nature Biomedical Engineering* 6 (2022): 741–753, https://doi.org/10.1038/s41551-021-00817-7.

32. P. Li, J. Zhang, H. Hayashi, et al., "Monolithic Silicon for High Spatiotemporal Translational Photostimulation," *Nature* 626 (2024): 990–998, https://doi.org/10.1038/s41586-024-07016-9.

33. J. Chen, Y. Liu, F. Chen, et al., "Non-Faradaic Optoelectrodes for Safe Electrical Neuromodulation," *Nature Communications* 15 (2024): 405, https://doi.org/10.1038/s41467-023-44635-8.

34. W. S. Kim, S. Hong, M. Gamero, et al., "Organ-specific, Multimodal, Wireless Optoelectronics for High-throughput Phenotyping of Peripheral Neural Pathways," *Nature Communications* 12 (2021): 157, https://doi.org/10.1038/s41467-020-20421-8.

35. C. H. Mac, G. L. T. Nguyen, D. T. M. Nguyen, et al., "Noninvasive Vagus Nerve Electrical Stimulation for Immune Modulation in Sepsis Therapy," *Journal of the American Chemical Society* 147 (2025): 8406–8421, https://doi.org/10.1021/jacs.4c16367.

36. Y. Sun, S. Chao, H. Ouyang, et al., "Hybrid Nanogenerator Based Closed-loop Self-powered Low-level Vagus Nerve Stimulation System for Atrial Fibrillation Treatment," *Science Bulletin* 67 (2022): 1284–1294.

37. F. Wang, L. Wang, X. Zhu, Y. Lu, and X. Du, "Neuron-Inspired Ferroelectric Bioelectronics for Adaptive Biointerfacing," *Advanced Materials* 37 (2025): 2416698, https://doi.org/10.1002/adma.202416698.

38. H. Song, M. Kim, E. Kim, et al., "Neuromodulation of the Peripheral Nervous System: Bioelectronic Technology and Prospective Developments," *BMEMat* 2 (2023): 12048.

39. S. Wang, Q. Zhao, J. Li, and X. Du, "Morphing-to-Adhesion Polysaccharide Hydrogel for Adaptive Biointerfaces," *ACS Applied Materials & Interfaces* 14 (2022): 42420–42429, https://doi.org/10.1021/acsami.2c10117.

40. F. Wang, M. Liu, C. Liu, et al., "Light-induced Charged Slippery Surfaces," *Science Advances* 8 (2022): abp9369.

41. F. Wang, X. Zhu, and X. Du, "Intelligent Poly(vinylidene fluoride)-Based Materials for Biomedical Applications," *Advanced Functional Materials* 35 (2025): 2500685, https://doi.org/10.1002/adfm.202500685.

42. L. Bao, X. J. Cui, M. Mortimer, X. Y. Wang, J. G. Wu, and C. Y. Chen, "The Renaissance of One-dimensional Carbon Nanotubes in Tissue Engineering," *Nano Today* 49 (2023): 101784, https://doi.org/10.1016/j.nantod.2023.101784.

43. L. Shan, Y. Xue, X. Chen, et al., "Mechanically Compliant and Impedance Matching Hydrogel Bioelectronics for Low-Voltage Peripheral Neuromodulation," *Advanced Materials* 38 (2025): 11014.

44. H. Hu, M. Nie, M. Galluzzi, X. Yu, and X. Du, "Mimosa-Inspired High-Sensitive and Multi-Responsive Starch Actuators," *Advanced Functional Materials* 33 (2023): 2304634, https://doi.org/10.1002/adfm.202304634.

45. H. Hu, C. Huang, M. Galluzzi, et al., "Editing the Shape Morphing of Monocomponent Natural Polysaccharide Hydrogel Films," *Research* 2021 (2021): 9786128, https://doi.org/10.34133/2021/9786128.

46. X. Du, H. Cui, Q. Zhao, J. Wang, H. Chen, and Y. Wang, "Inside-out 3D Reversible Ion-triggered Shape-morphing Hydrogels," *Research* 2019 (2019): 6398296.

47. M. Yu, C. Wang, H. Cui, et al., "Self-Closing Stretchable Cuff Electrodes for Peripheral Nerve Stimulation and Electromyographic Signal Recording," *ACS Applied Materials & Interfaces* 15 (2023): 7663–7672, https://doi.org/10.1021/acsami.2c15808.

48. J. Wang, Q. Zhao, Y. Wang, Q. Zeng, T. Wu, and X. Du, "Self-Unfolding Flexible Microelectrode Arrays Based on Shape Memory Polymers," *Advanced Materials Technologies* 4 (2019): 1900566.

49. X. Du, H. Cui, B. Sun, et al., "Photothermally Triggered Shape-Adaptable 3D Flexible Electronics," *Advanced Materials Technologies* 2 (2017): 1700120, https://doi.org/10.1002/admt.201700120.

50. H. Yuk, C. E. Varela, C. S. Nabzdyk, et al., "Dry Double-sided Tape for Adhesion of Wet Tissues and Devices," *Nature* 575 (2019): 169–174, https://doi.org/10.1038/s41586-019-1710-5.

51. C. M. Costa, V. F. Cardoso, P. Martins, et al., "Smart and Multifunctional Materials Based on Electroactive Poly(vinylidene fluoride): Recent Advances and Opportunities in Sensors, Actuators, Energy, Environmental, and Biomedical Applications," *Chemical Reviews* 123 (2023): 11392–11487, https://doi.org/10.1021/acs.chemrev.3c00196.

52. S. Chakraborty, I. C. Liao, A. Adler, and K. W. Leong, "Electrohydrodynamics: a Facile Technique to Fabricate Drug Delivery Systems," *Advanced Drug Delivery Reviews* 61 (2009): 1043–1054, https://doi.org/10.1016/j.addr.2009.07.013.

53. M. Peng, Q. Zhao, A. Chai, Y. Wang, M. Wang, and X. Du, "A Ferroelectric Living Interface for Fine-tuned Exosome Secretion toward Physiology-mimetic Neurovascular Remodeling," *Matter* 8 (2025): 101901.

54. S. Marom and E. Marder, "A Biophysical Perspective on the Resilience of Neuronal Excitability across Timescales," *Nature Reviews Neuroscience* 24 (2023): 640–652, https://doi.org/10.1038/s41583-023-00730-9.

55. G. Batsikadze, V. Moliadze, W. Paulus, M. F. Kuo, and M. A. Nitsche, "Partially Non-Linear Stimulation Intensity-Dependent Effects of Direct Current Stimulation on Motor Cortex Excitability in Humans," *The Journal of Physiology* 591 (2013): 1987–2000, https://doi.org/10.1113/jphysiol.2012.249730.

56. Y. Jiang, X. Li, B. Liu, et al., "Rational Design of Silicon Structures for Optically Controlled Multiscale Biointerfaces," *Nature Biomedical Engineering* 2 (2018): 508–521, https://doi.org/10.1038/s41551-018-0230-1.

57. E. Molokanova, T. Zhou, P. Vasupal, et al., "Non-genetic Neuromodulation with Graphene Optoelectronic Actuators for Disease Models, Stem Cell Maturation, and Biohybrid Robotics," *Nature Communications* 16 (2025): 7499, https://doi.org/10.1038/s41467-025-62637-6.

58. Z. Q. Liu, X. Y. Chen, W. J. Ma, et al., "Suppression of Lipopolysaccharide-Induced Sepsis by Tetrahedral Framework Nucleic Acid Loaded with Quercetin," *Advanced Functional Materials* 32 (2022): 2204587, https://doi.org/10.1002/adfm.202204587.

59. V. A. Pavlov and K. J. Tracey, "The Vagus Nerve and the Inflammatory Reflex—Linking Immunity and Metabolism," *Nature Reviews Endocrinology* 8 (2012): 743–754, https://doi.org/10.1038/nrendo.2012.189.

60. D. Nelidova, R. K. Morikawa, C. S. Cowan, et al., "Restoring Light Sensitivity Using Tunable near-infrared Sensors," *Science* 368 (2020): 1108–1113, https://doi.org/10.1126/science.aaz5887.

61. W. J. de Jonge, E. P. van der Zanden, F. O. The, et al., "Stimulation of the Vagus Nerve Attenuates Macrophage Activation by Activating the Jak2-STAT3 Signaling Pathway," *Nature Immunology* 6 (2005): 844–851, https://doi.org/10.1038/ni1229.

62. Q. Zhao, J. Wang, Y. Wang, H. Cui, and X. Du, "A Stage-specific Cell-manipulation Platform for Inducing Endothelialization on Demand," *National Science Review* 7 (2020): 629–643, https://doi.org/10.1093/nsr/nwz188.

63. R. Feiner and D. Tal, "Tissue–electronics Interfaces: from Implantable Devices to Engineered Tissues," *Nature Reviews Materials* 3 (2017): 17076, https://doi.org/10.1038/natrevmats.2017.76.

64. G. Schalk, P. Brunner, B. Z. Allison, et al., "Translation of Neurotechnologies," *Nature Reviews Bioengineering* 2 (2024): 637–652, https://doi.org/10.1038/s44222-024-00185-2.

65. F. Wang, M. Liu, C. Liu, et al., "Light Control of Droplets on Photo-induced Charged Surfaces," *National Science Review* 10 (2023): nwac164, https://doi.org/10.1093/nsr/nwac164.

66. C. Liu, F. Wang, and X. Du, "Self-powered Electrostatic Tweezer for Adaptive Object Manipulation," *Device* 2 (2024): 100465.

67. F. Wang, C. Liu, Z. Dai, et al., "Photopyroelectric Tweezers for Versatile Manipulation," *The Innovation* 6 (2025): 100742, https://doi.org/10.1016/j.xinn.2024.100742.

68. L. Zhang, P. Naumov, X. Du, Z. Hu, and J. Wang, "Vapomechanically Responsive Motion of Microchannel-Programmed Actuators," *Advanced Materials* 29 (2017): 1702231, https://doi.org/10.1002/adma.201702231.

69. L. H. Wang, S. L. Jacques, and L. Q. Zheng, "MCML—Monte Carlo Modeling of Light Transport in Multi-layered Tissues," *Computer Methods and Programs in Biomedicine* 47 (1995): 131–146, https://doi.org/10.1016/0169-2607(95)01640-F.

Supporting Information

Additional supporting information can be found online in the Supporting Information section.

Supporting File 1: adma73023-sup-0001-SuppMat.docx.

Supporting File 2: adma73023-sup-0002-VideoS1.mp4.

Supporting File 3: adma73023-sup-0003-VideoS2.avi.

Supporting File 4: adma73023-sup-0004-VideoS3.avi.

Supporting File 5: adma73023-sup-0005-VideoS4.avi.

Supporting File 6: adma73023-sup-0006-VideoS5.avi.

Supporting File 7: adma73023-sup-0007-VideoS6.mp4.

Supporting File 8: adma73023-sup-0008-VideoS7.mp4.